

# Evaluation of Algorithms for Intracranial EEG (iEEG) Source Imaging of Extended Sources: Feasibility of Using iEEG Source Imaging for Localizing Epileptogenic Zones in Secondary Generalized Epilepsy

Jae-Hyun Cho · Seung Bong Hong · Young-Jin Jung ·  
Hoon-Chul Kang · Heung Dong Kim · Minah Suh ·  
Ki-Young Jung · Chang-Hwan Im

Received: 26 December 2010 / Accepted: 22 February 2011 / Published online: 3 March 2011  
© Springer Science+Business Media, LLC 2011

**Abstract** Precise identification of epileptogenic zones in patients with intractable drug-resistant epilepsy is critical for successful epilepsy surgery. Numerous source-imaging algorithms for localizing epileptogenic zones based on scalp electroencephalography (EEG) and magnetoencephalography (MEG) have been developed and validated in simulation and experimental studies. Recently,

intracranial EEG (iEEG)-based imaging of epileptogenic sources has attracted interest as a promising tool for presurgical evaluation of epilepsy; however, most iEEG studies have focused on localization of epileptogenic zones in focal epilepsy. In the present study, we investigated whether iEEG source imaging is a useful supplementary tool for identifying extended epileptogenic sources in secondary generalized epilepsy such as Lennox-Gastaut syndrome (LGS). To this end, we applied four different cortical source imaging algorithms, namely minimum norm estimation (MNE), low-resolution electromagnetic tomography (LORETA), standardized LORETA (sLORETA), and  $L_p$ -norm estimation ( $p = 1.5$ , referred to as  $L_{p1.5}$ ), to artificial iEEG datasets generated assuming various source sizes and locations. We also applied these four algorithms to clinical ictal iEEG recordings acquired from a pediatric patient with LGS. Interestingly, the traditional MNE algorithm outperformed the other imaging algorithms in most of our experiments, particularly in cases when larger-sized sources were activated. Although sLORETA outperformed both LORETA and  $L_{p1.5}$ , its performance was not as good as that of MNE. Compared to the other algorithms, the performance of  $L_{p1.5}$  decayed most rapidly as the source size increased. Our findings suggest that iEEG source imaging using MNE is a promising auxiliary tool for the identification of epileptogenic zones in secondary generalized epilepsy. We anticipate that our results will provide useful guidelines for selection of an appropriate imaging algorithm for iEEG source imaging studies.

Jae-Hyun Cho and Seung Bong Hong contributed equally to this study (co-first authors).

**Electronic supplementary material** The online version of this article (doi:10.1007/s10548-011-0173-2) contains supplementary material, which is available to authorized users.

J.-H. Cho · Y.-J. Jung  
Department of Biomedical Engineering, Yonsei University,  
Wonju, South Korea

S. B. Hong  
Department of Neurology, Samsung Medical Center,  
Sungkyunkwan University, Seoul, Korea

H.-C. Kang · H. D. Kim  
Department of Pediatrics, Yonsei University College  
of Medicine, Seoul, Korea

M. Suh  
Department of Biological Science, Sungkyunkwan University,  
Suwon, Korea

K.-Y. Jung  
Department of Neurology, Korea University College  
of Medicine, Seoul, Korea

C.-H. Im (✉)  
Department of Biomedical Engineering, Hanyang University,  
17 Haengdang-dong, Seongdong-gu, Seoul 133-791,  
South Korea  
e-mail: ich@hanyang.ac.kr

**Keywords** Cortical source imaging · Localization of epileptogenic zone · Lennox-Gastaut syndrome · Intracranial electroencephalography · Ictal epileptiform activity · Inverse problem

## Introduction

Precise identification of epileptogenic zones is critical for successful surgical treatment of patients with intractable drug-resistant epilepsy. To estimate epileptogenic zones, various neuroimaging techniques have been utilized such as video scalp electroencephalography (EEG), magnetoencephalography (MEG), ictal/interictal single photon emission computed tomography (SPECT), positron emission tomography (PET), and functional magnetic resonance imaging (fMRI) triggered by simultaneously recorded EEG (Krakow et al. 1999; Oliveira et al. 1999; Kim et al. 2002; Wu et al. 2006). Among the neuroimaging techniques listed above, scalp EEG and MEG have been extensively used for noninvasive identification of epileptogenic zones because these techniques can record both ictal and interictal epileptiform activities with millisecond temporal resolution. Despite their excellent temporal resolution, however, the spatial resolutions provided by EEG and MEG are not comparable to those provided by fMRI or PET due to limited spatial sampling, the volume conduction effect, and additive noise/artifacts. The spatial resolutions of both EEG and MEG can be substantially improved by performing source imaging or by solving an inverse problem to estimate the EEG or MEG sources (Nunez and Srinivasan 2006). Because EEG and MEG source imaging can help to delineate brain regions where epileptiform activities are generated, it has become a well-established tool for the clinical diagnosis of epilepsy.

However, despite the recent rapid developments in source imaging technology, noninvasive imaging modalities such as EEG and MEG have not been used directly to localize surgical resection areas. They have instead been used as supplementary tools to determine the locations of intracranial EEG (iEEG) electrodes because of their limited spatial resolution. Indeed, in modern clinical neurophysiology, iEEG recorded from subdural electrodes is regarded as the most reliable modality for determining surgical resection areas prior to epilepsy surgery (Binnie et al. 1994; Behrens et al. 1994; Dubeau and McLachlan 2000; Rosenow and Lüders 2001; Pondal-Sordo et al. 2007).

Recently, several groups have reported that source imaging methods can also be applied to iEEG recordings, and have demonstrated that iEEG source imaging may provide auxiliary information on the underlying brain activities associated with epilepsy. Fuchs et al. (2007) first suggested the possibility of using intracranial recordings for imaging underlying brain activities. They applied the minimum norm estimation (MNE) method to simulated electrocorticogram (ECoG) datasets and interictal iEEG recordings, and demonstrated that iEEG source imaging can localize brain electrical sources with fairly high localization accuracy. They also compared different head

volume conductor models and showed that boundary element method (BEM) models provided more accurate source estimates than the spherical head model. Zhang et al. (2008) also applied a 3D source estimation method based on MNE and finite element method (FEM) models to iEEG recordings and reported that not only did iEEG source imaging provide higher spatial resolution, but it was also able to better localize deep brain sources compared to conventional EEG source imaging. Dümpelmann et al. (2009) compared the localization accuracies of two different source imaging methods, multiple signal classification (MUSIC) and MNE, using simulated iEEG data and actual iEEG data recorded from epilepsy patients. They reported that both algorithms performed similarly when the neuronal sources were in shallow cortical areas; however, MUSIC performed better than MNE when sources were located in relatively deeper brain areas.

Previous studies have demonstrated that iEEG source imaging is particularly useful for the presurgical evaluation of intractable epilepsy. For example, misidentification of subdural grid or strip electrode locations can lead to wrong or inaccurate localization of epileptogenic foci; however, iEEG source imaging has the potential to localize epileptogenic sources generated outside the subdural electrodes (Kim et al. 2010). Moreover, iEEG source imaging results can be used to confirm the conclusions drawn from visual inspection of ictal or interictal iEEG recordings (Kim et al. 2010), as defining and localizing epileptogenic zones can be difficult, particularly when rapidly propagating epileptiform activities exist and the epileptogenic zones are not readily discriminable from the propagated irritative zones (Wilke et al. 2010). Most importantly, it is obvious that the use of additional imaging modalities and imaging results should provide more supplementary information for determining surgical resection areas.

It is noteworthy that all previous studies on iEEG source imaging focused only on the localization of epileptogenic zones in focal epilepsy. However, in some patients with secondary generalized epilepsy such as Lennox-Gastaut syndrome (LGS), localization of epileptogenic zones is also critical for surgical treatment, as a number of recent studies have demonstrated that some focal epileptogenic zones are likely to generate the generalized epileptiform discharges in many types of generalized epilepsy (Ag-hakhani et al. 2004; Archer et al. 2003; Gotman et al. 2005; Salek-Haddadi et al. 2003; Berman et al. 2010; Bai et al. 2010). LGS is an epileptic syndrome with intractable, multiple seizure types including tonic, atonic, myoclonic, and atypical absence seizures (Heiskala 1997). Some patients with LGS have focal lesions that contribute to secondary generalized epileptic encephalopathy; these focal lesions (generally more extended than those of typical focal epilepsy) are generally identified based on interictal

iEEG characteristics because of their generalized ictal iEEG discharges. Recent studies have reported successful outcomes of respective epilepsy surgery for children with LGS, despite abundant generalized and multiregional EEG abnormalities (Wyllie et al. 2007; Lee et al. 2010). However, additional refinement techniques to confirm the locations of epileptogenic zones are still required to facilitate successful epilepsy surgery. To the best of our knowledge, source imaging of ictal or interictal discharges of secondary LGS with abundant bisynchronous epileptiform discharges has not previously been performed with any electrophysiological imaging modalities, including EEG, MEG, and iEEG. In the present study, we therefore investigated if iEEG source imaging could be used to successfully identify epileptogenic zones in secondary generalized epilepsy and evaluated various algorithms for iEEG source imaging of extended sources.

## Materials and Methods

### Geometric Modeling for Computer Simulations

In our simulation study, a realistic geometry head model was considered for accurate forward calculations. Two-layer tessellated boundary surfaces, consisting of an inner skull boundary and epicortical surface, were generated using CURRY6 for Windows (Compumedics Neuroscan, El Paso, TX, USA). A total of 4,939 surface nodes and 9,874 boundary elements were generated from T1-weighted MR images of a standard brain atlas (Colin27: <http://imaging.mrc-cbu.cam.ac.uk/downloads/Colin>) provided by the Montreal Neurological Institute (MNI). We used conductivity values of 1.79 and 0.33 S/m for the CSF and brain compartments, respectively (Oostendorp et al. 2000). The volume conduction effect outside the inner skull boundary was ignored in this study due to the very low electrical conductivity of the human skull layer (Fuchs et al. 2007).

Because synchronously activated pyramidal cortical neurons, which are located perpendicularly on the cortical surface, are widely believed to be the main EEG and MEG generators, many recent studies have adopted this physiological phenomenon as a basic anatomical constraint in EEG or MEG source imaging (Dale and Sereno 1993; Kincses et al. 1999; Dale et al. 2000; Babiloni et al. 2003, 2005). To impose this anatomical constraint, numerous dipolar sources were placed on the cortical surface that was tessellated using CURRY6. The generated cortical surface model consisted of 34,924 surface vertices and 69,880 triangular elements.

To simulate subdural grid electrode positions, we referred to the typical subdural grid placements used for

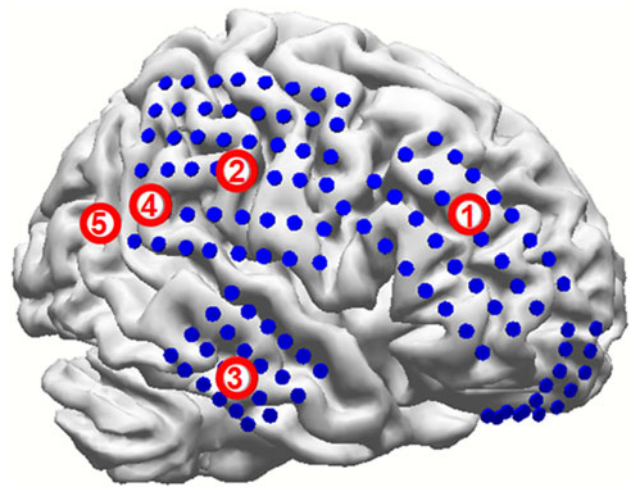


**Fig. 1** Locations of subdural grid electrodes coregistered with the tessellated cortical surface, and the locations of artificial extended sources. Filled blue circles indicate the subdural electrodes. The total number of electrodes was 120, and five separate compartments were located in the frontal lobe ( $8 \times 2$  and  $8 \times 4$  grids), parietal lobe ( $8 \times 2$  and  $8 \times 4$  grids), and temporal lobe ( $4 \times 6$  grid). The numbered red circles indicate the locations of centers of artificial extended sources. The number in each circle represents the source index

LGS patients and generated 120 grid electrodes covering the right frontal area ( $8 \times 2$  and  $8 \times 4$  grids), right parietal area ( $8 \times 2$  and  $8 \times 4$  grids), and temporal area ( $4 \times 6$  grid), as depicted in Fig. 1. After generating the head geometry model, a first-order, node-based boundary element method (BEM) was applied to construct a leadfield matrix, which relates cortical sources to the potential at the iEEG electrodes (Fuchs et al. 2007).

### Simulated iEEG Data and Simulation Protocols

To simulate realistic iEEG data, we first placed cortical source patches on the tessellated cortical surface. The patches were made of a set of dipoles whose orientations were perpendicular to the cortical surface. The centers of the cortical source patches are depicted in Fig. 1, where sources 1, 2, and 3 are located below the subdural grids, source 5 is located outside the grids, and source 4 is located at the border. We simulated various iEEG datasets assuming different patch sizes and locations, which are described in detail below. To define the sizes of the patches, we evaluated the geodesic distances from the seed points (center locations; sources 1–5 depicted in Fig. 1) to all cortical vertices (Surazhsky et al. 2005). The radii of the simulated source patches were 10, 20, 30, 40, 50, and 60 mm. We assumed anisotropic source patches that had a source intensity value of 1 at the center of each patch and then decreased monotonically as the geodesic distance

from the center location increased. Source intensity values were set to 0 outside the border of each patch. After calculating the electric potential at each subdural electrode by solving a forward problem, we added white Gaussian noise. The signal-to-noise ratio (SNR) was set to 20, considering that subdural grid electrodes can measure neuronal signals with high SNR values (Zhang et al. 2008). All computations were performed using an in-house program coded with Matlab 2009a (Mathworks, Inc., USA). Figure 2 summarizes the procedures used for the simulation study. The pre-calculated leadfield matrix was used to generate artificial iEEG datasets as well as to reconstruct cortical source distributions.

We then applied four different cortical source-imaging algorithms to the artificial iEEG datasets generated assuming various simulation conditions. We assumed the nine different cases described below; Case I: A single source patch was placed in the right posterior prefrontal lobe (below the grid; source location 1); Case II: A single source patch was placed in the inferior parietal lobule (below the grid; source location 2); Case III: A single source patch was placed in the inferior temporal gyrus (below the grid; source location 3); Case IV: A single source patch was placed in the inferior parietal lobule (below the edge of the grid; source location 4); Case V: A single source patch was placed in a relatively posterior area of the inferior parietal lobule (outside the grid; source location 5); Case VI: Two source patches were placed at source locations 1 and 2; Case VII: Two source patches were placed at source locations 2 and 3; Case VIII: Two source patches were placed at source locations 1 and 3; and Case IX: Three source patches were placed at source locations 1, 2, and 3. For each of the cases listed above, six different patch sizes were tested.

## Algorithms for iEEG Cortical Source Imaging

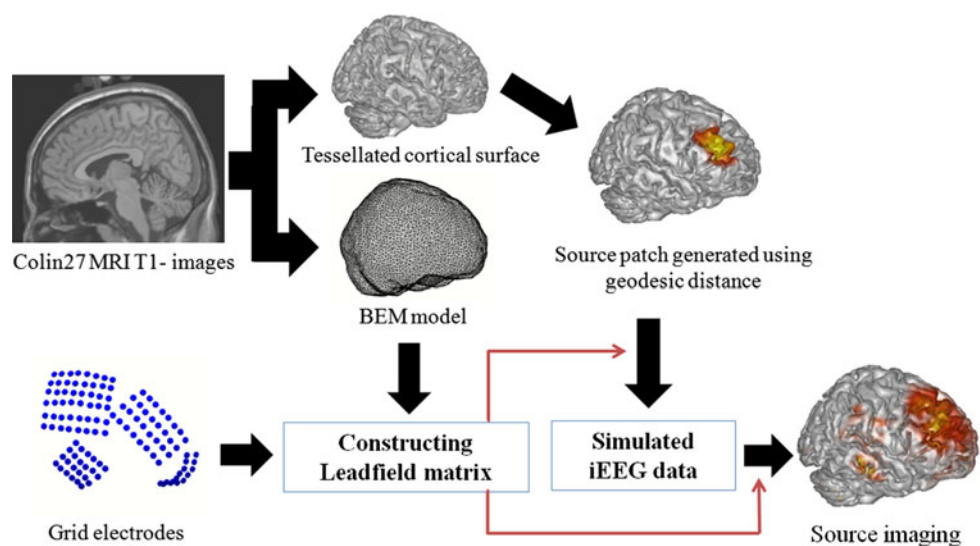
To evaluate different source imaging algorithms, we applied four different cortical source imaging algorithms: MNE,  $L_p$ -norm ( $p = 1.5$ ), low-resolution electromagnetic tomography (LORETA), and standardized LORETA (sLORETA), to both simulated and experimental datasets. We used CURRY6 software for source imaging and exported the resultant source distributions to ASCII data files for further analyses. BEM was used for the forward calculations in both the simulation and experimental data analyses. Because the technical details of each imaging algorithm are beyond the scope of this article, we provide a brief summary of the basic concepts of each algorithm below. Cortical orientation constraint was imposed for the simulated iEEG data analyses, whereas it was not imposed for the practical iEEG data analyses due to the incomplete segmentation of the cortical surface model.

The MNE algorithm is one of the earliest algorithms developed for cortical source imaging and is based on the  $L_2$ -norm minimization. The general form of the function to be minimized can be expressed as

$$\min\{\|\mathbf{L}\mathbf{J} - \mathbf{x}\|_2 + \lambda\|\mathbf{W}\mathbf{J}\|_2\}, \quad (1)$$

where  $\mathbf{L}$  is an  $m \times n$  leadfield matrix that relates  $m$  sensors and  $n$  sources,  $\mathbf{J}$  is an  $n \times 1$  vector ( $3n \times 1$  when an orientation constraint is not imposed) representing the strength of  $n$  sources,  $\|\cdot\|_2$  represents the Euclidean norm,  $\lambda$  is a regularization parameter that controls the weight given to the minimization of the side constraint, and  $\mathbf{W}$  is a weighting matrix and is generally set to an identity matrix when there is no a priori information (Wang et al. 1992). The general solution of (1) can be expressed in the form of linear equations and thus can be readily obtained without

**Fig. 2** A schematic illustration of the procedures used in the simulation studies. The cortical surface and BEM models were generated from Colin27 MRI and coregistered with grid electrodes. The pre-calculated leadfield matrix was used to generate artificial iEEG datasets as well as to reconstruct cortical source distributions. Four different cortical source-imaging algorithms were evaluated using the simulated iEEG datasets



any iterative processes (please refer to Liu et al. 2002 for various forms of the linear inverse operators).

The  $L_p$ -norm estimation can be regarded as a general form of MNE that uses  $L_p$ -norm ( $1 \leq p \leq 2$ ) instead of a Euclidean norm ( $p = 2$ ) in its formulations. The general form of the function to be minimized is expressed as

$$\min \left\{ \|\mathbf{LJ} - \mathbf{x}\|_p - \lambda \|\mathbf{WJ}\|_p \right\}, \quad (2)$$

where  $\|\cdot\|_p$  is a norm of order  $p$ , and nonlinear iterative processes are generally adopted to obtain the solution of (2) (Fuchs et al. 1999). In EEG and MEG source imaging, the use of small  $P$  values generally results in focal source estimates (Fuchs et al. 1999) compared to those obtained from MNE. In the present study, we evaluated  $L_{1.5}$ -norm ( $p = 1.5$ ) estimation, which we refer to as  $L_{p1.5}$  hereafter.

The LORETA algorithm was developed by Pascual-Marqui et al. (1994) and has been applied extensively in a variety of practical EEG and MEG source imaging applications. LORETA assumes that neuronal electric activities have maximum synchronization between neighboring neuron populations by introducing a Laplacian operator in its formulation. In LORETA, the function to be minimized is described as

$$\min \left\{ \|\mathbf{LJ} - \mathbf{x}\|_2 + \lambda \|\mathbf{BWJ}\|_2 \right\}, \quad (3)$$

where  $\mathbf{B}$  is the discrete Laplacian operator that plays a role in obtaining smooth solutions (Pascual-Marqui et al. 1994). We used a Euclidean norm based on a previous EEG-based simulation study that reported that LORETA with a Euclidean norm was more appropriate for epileptogenic source localization than LORETA with an  $L_p$  norm (Grova et al. 2006).

sLORETA (Pascual-Marqui 2002) is able to compute statistical source images by performing an inverse weighting of the LORETA imaging results and their estimated variances. Because sLORETA provides statistical values, it is particularly useful for dealing with multiple subjects/group datasets. For all the source imaging algorithms, the regularization parameter was determined by  $\chi^2$  criterion method implemented in CURRY (Wischmann et al. 1992; Bai et al. 2007).

### Quantitative Evaluation of Simulation Results

The accuracy of the cortical source imaging results was evaluated by using two assessment criteria: the correlation coefficient (CC) and the error distance (ED).

The correlation coefficient (CC) quantifies the concordance between the simulated original cortical source profiles and the estimated source distributions (Zhang et al. 2006) and was calculated using the following equation:

$$CC = \frac{\sum_{i=1}^N (X_i - \bar{X})(E_i - \bar{E})}{\sqrt{\sum_{i=1}^N (X_i - \bar{X})^2 \sum_{i=1}^N (E_i - \bar{E})^2}}, \quad (4)$$

where  $N$  is the total number of source locations over the tessellated cortical surface,  $X_i$  is the simulated source intensity at the  $i$ -th cortical vertex,  $\bar{X}$  is the mean value of  $X_i$ s,  $E_i$  is the estimated source intensity at the  $i$ -th cortical vertex, and  $\bar{E}$  is the mean value of  $E_i$ s. The CC value can range from  $-1$  (negative correlation) to  $1$  (positive correlation). We did not apply any threshold values as well as did not use normalized current intensities for the CC calculation.

The error distance (ED) (Yao and Dewald 2005) quantifies the distance between the original and estimated source locations and was defined as

$$ED = \frac{1}{N_I} \sum_i \min_j \{ \|\tilde{d}_i - s_j\| \} + \frac{1}{N_J} \sum_{j \in J} \min_i \{ \|s_j - \tilde{d}_i\| \}, \quad (5)$$

where  $s_j$  is the actual source location,  $\tilde{d}_i$  is the estimated source location, subscripts  $i$  and  $j$  are the indices of locations of estimated and actual sources, respectively,  $J$  is a dataset consisting of all the real sources that were not identified by the source imaging methods, and  $N_I$  and  $N_J$  are the total numbers of estimated and the undetected sources, respectively. The estimated source location was defined as the location where the current strength is larger than a threshold, which was set as the value corresponding to top 1% of the reconstructed current density. In the Eq. 1, the first term evaluates the mean of the distance from each estimated source to its closest actual source and the second term evaluates the mean of the distance from each of the undetected actual sources to the closest estimated sources (Yao and Dewald 2005).

### Source Imaging of Ictal iEEG Acquired from an LGS Patient

We applied the cortical source imaging algorithms used for the simulation study to a practical iEEG dataset recorded from a pediatric patient with intractable LGS. The subject (LYS) was a 3-year-old boy with severe mental impairment (Intelligence Quotient (IQ) of 25) who had suffered from refractory epilepsy since 7 months of age. Two types of seizures were observed in this subject—generalized tonic spasms and head drops—and none of the available anti-epileptic medications could suppress his seizures. In this patient's pre-surgical evaluation at the age of 3 years, MRI findings were normal. FDG-PET scans did not reveal any asymmetric hypometabolism, but SISCOM, which was obtained using a slow ictal SPECT injection protocol,

lateralized consistently to the right frontotemporal area with an epileptogenic focus. Continuous video EEG monitoring showed frequent, generalized, slow spikes and waves and generalized paroxysmal fast activities, as well as localized epileptiform discharges or bisynchronous sharp waves located predominantly in the right frontotemporal areas. Ictal EEG showed generalized slow waves followed by low-voltage fast activities during generalized tonic seizures or head drops, but did not aid in the lateralization of the epileptogenic area. Based on the results of a Phase I study and ictal/interictal iEEG monitoring, the patient underwent a right frontal resection at 3 years of age at Severance Children's Hospital and was free of seizures for 2.5 years before his seizures recurred at 6 years of age. The posterior margin of the pre-resection site was further resected at the same hospital, and the patient has been free of seizures for 1.6 years (see Fig. 9a in advance for the final resection areas marked on the electrode grids). Pathology revealed focal cortical dysplasia (CD)-type epilepsy. The EEG after reoperation showed nearly normalized background activity and no epileptiform discharges. This study was approved by the Institutional Review Board of Severance Hospital, and the patient's parents provided written consent for the study.

The ictal iEEG data were recorded using a multichannel digital EEG acquisition system (Telefactor, Grass Technologies) at a sampling rate of 200 Hz. The locations of the grid subdural electrodes were localized and lateralized based on multimodal neuroimaging results from video EEG monitoring, MRI, PET, and SPECT as well as the ictal semiology. The number of subdural electrodes was 104 and their positions are depicted in Fig. 9a. The recorded iEEG data were reviewed by an epileptologist; two distinct seizure events were selected for iEEG source imaging. Seizure onset times were identified visually by the epileptologist with the aid of video monitoring. No specific pre-processing procedures except for baseline correction and 60 Hz notch filtering were applied to the raw iEEG data.

The LGS patient's BEM model and cortical surface model were extracted and tessellated from structural MR images acquired from the patient before epilepsy surgery using CURRY6 software. The BEM model consisted of the inner skull boundary and epicortical surface, and comprised a total of 7,512 elements. The tessellated cortical surface consisted of 14,785 vertices and 29,626 elements. The locations of subdural grid electrodes were extracted from the patient's CT images and coregistered on the epicortical surface of the BEM model. We used conductivity values of 1.79 and 0.33 S/m for the CSF and brain compartments, respectively, as in the simulation experiments. We used CURRY6 software for source imaging and exported the resultant source distributions to

ASCII data files for further analyses. To quantitatively compare the results of different source imaging algorithms, we evaluated the degree of focalization (DF), which quantifies how much of the reconstructed source is contained in the reference source (Im et al. 2003). This validation metric can range in value from 0 to 100 and is defined as follows:

$$DF = \frac{\sum_{i \in \Pi} j_i^2}{\sum_{i \in \Omega} j_i^2} \times 100(\%), \quad (6)$$

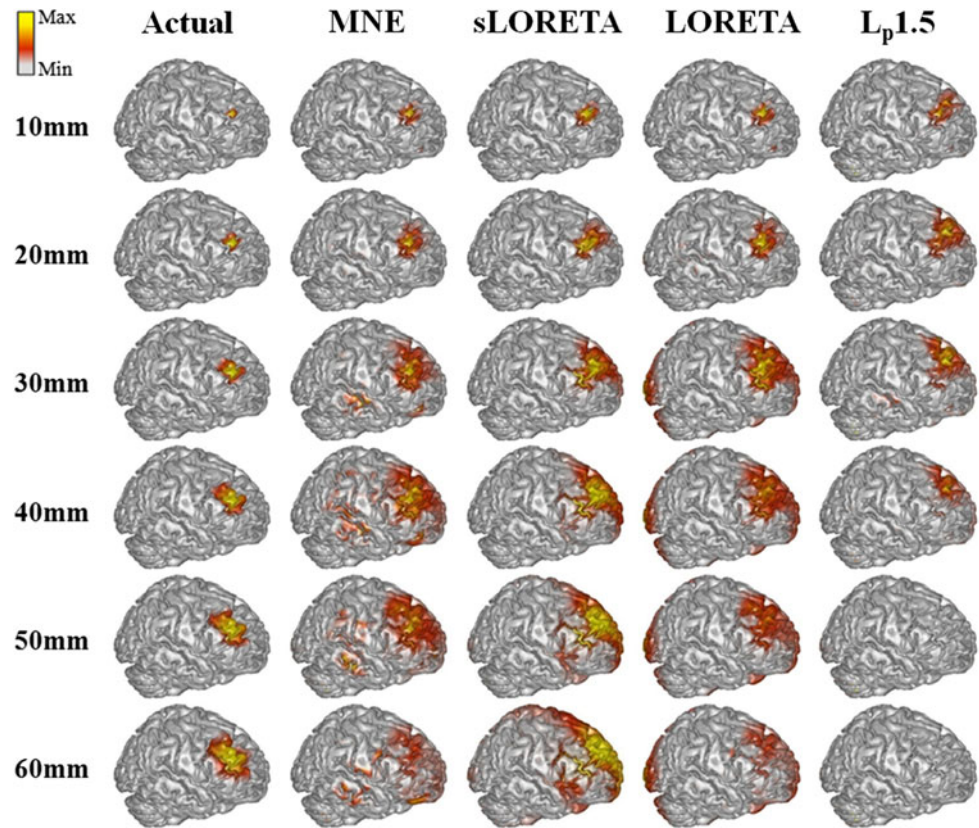
where  $j_i$  represents the source intensity at the  $i$ th cortical vertex,  $\Omega$  denotes the whole source space, and  $\Pi$  denotes the reference source space, which is the surgical resection area in this study. We could apply the DF measure only in the patient study as we could define the reference source space; whereas this measure could not be applied to our simulation studies because the reference source space could not be defined for the anisotropic source patches having certain distributions.

## Results

### Simulation Results: Visual Inspection of Estimated Source Images

Some example source images reconstructed for the nine different source configurations are shown in Figs. 3, 4, 5 and 6. All results were normalized to each maximum and displayed with a threshold of 10% of the maximum value. Figure 3 shows the source imaging results when a single simulated source patch was placed below the subdural grid electrodes (in the right posterior prefrontal lobe; case I). We frequently observed that the source localization accuracy decreased as the size of the simulated source patch increased. When the radius of the source patch was below 20 mm, all algorithms were able to localize the location of the simulated source fairly well. The sLORETA source estimates contained the location of the simulated source when the radius of the source patch was less than 20 mm, but the source estimate gradually moved in the anterior direction and was located further outside of the subdural grid as the patch size increased. The LORETA results showed similar distributions to those of MNE around the simulated source patch area, but strong spurious activities were observed around the visual cortex area when the radius of the source patch was greater than 30 mm. Lp1.5 showed reasonable source estimates when the radius of the source patch was less than 20 mm, but the peak source activity shifted away from the actual locations as the source radius increased, and even vanished from the right hemisphere when the source radius exceeded 50 mm. According to visual inspection of the results, MNE showed the best

**Fig. 3** Source estimates when a single source patch was placed in the right posterior prefrontal lobe (below the subdural grid; Case I). The first column shows the actual simulated sources with various patch sizes. The other four columns show the source imaging results reconstructed using four different cortical source imaging algorithms—MNE, sLORETA, LORETA, and Lp1.5, respectively. All results were normalized to each maximum and displayed with a threshold of 10%. The above explanations are valid for all results depicted in Figs. 3, 4, 5, 6, and 7



performance of the four algorithms. The source estimates of MNE maintained the peak source activities around the actual patch locations until the patch radius became 50 mm. Furthermore, the intensity of the spurious source activities was less when MNE was used than when LORETA was used. In cases when single source patches were placed in the inferior parietal lobule (Case II) and inferior temporal gyrus (Case III), both below the subdural grid electrodes, similar trends were observed to those seen for Case I in that (1) when the radius of the source patch was small, most of the algorithms were able to localize the locations of the simulated sources fairly well; (2) the source localization accuracy decreased as the size of the simulated source patch increased; (3) relatively larger spurious activities were generated by sLORETA and LORETA in the case of large patch sizes, compared to MNE; (4) Lp1.5 did not successfully localize the actual source locations even for small source patches; and (5) despite the fact that some spurious source activities outside of the subdural grid were seen in the MNE results when the source patch radius was larger than 40 mm, MNE appeared to better reconstruct the original source locations than the other algorithms (these results are shown in the Supplementary figures S1 and S2).

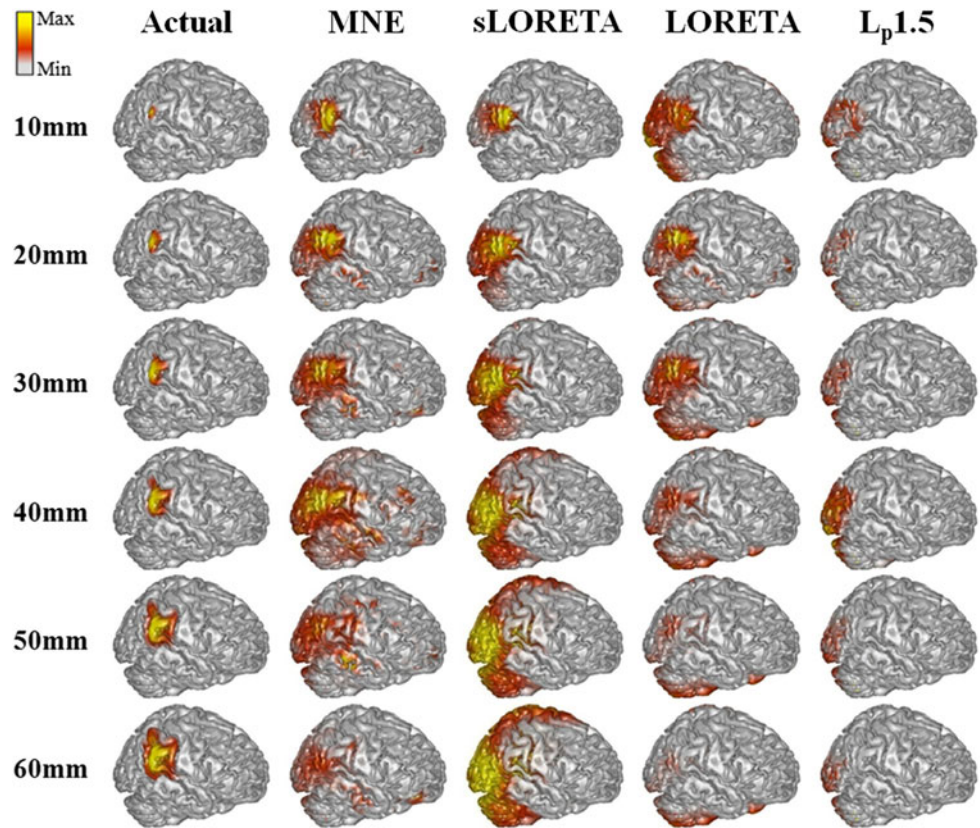
Figure 4 shows the source estimates when a single source patch was placed in the inferior parietal lobule

below the edge of the subdural grid (Case IV). In this case, MNE also showed the best performance of the four algorithms; however, more spurious source activities as well as broader cortical areas were seen in the MNE results than in the previous cases in which the simulated source patch was placed below the subdural grids. The other three algorithms showed similar tendencies. Both sLORETA and LORETA estimated source distributions away from the actual source locations when the patch radius was larger than 30 mm, which is worse than the previous results shown in Fig. 3. Lp1.5 was not able to correctly localize the actual source locations for any patch size.

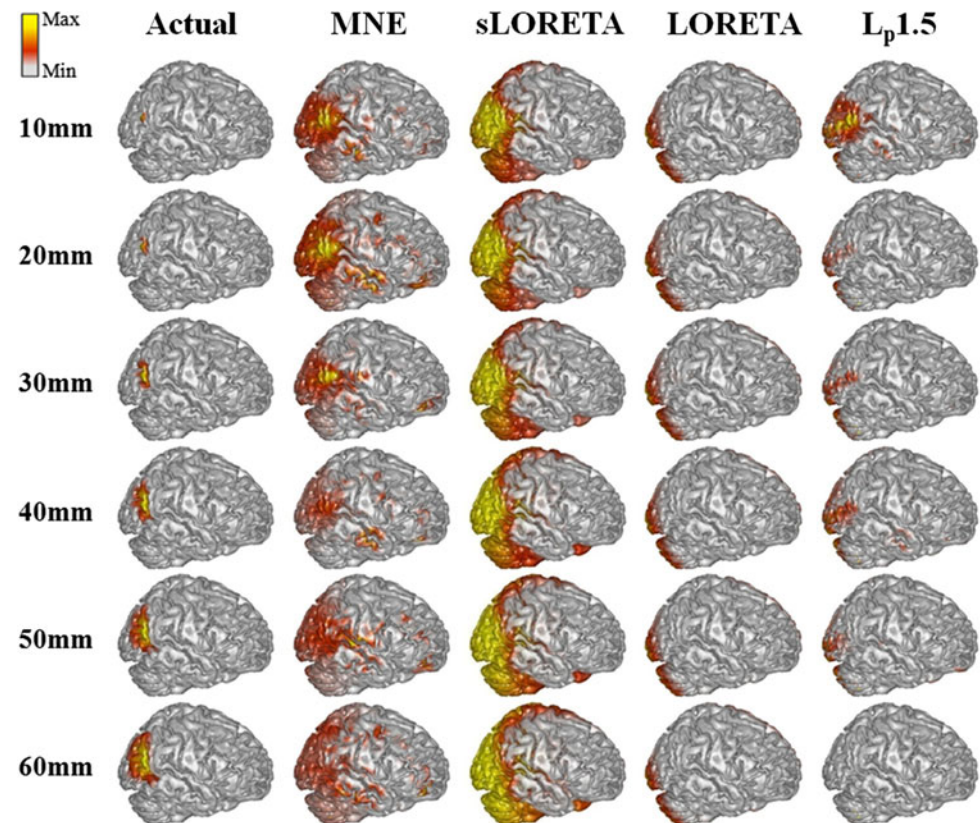
Figure 5 shows the source estimates when a single source patch was placed outside the subdural grid in a relatively posterior area of the inferior parietal lobule (Case V). Both MNE and sLORETA estimated broader source distributions with more spurious sources than those seen for any of the previous cases. Neither LORETA nor Lp1.5 was able to accurately localize the actual source locations, and the results were far worse than those obtained using MNE and sLORETA. Consistent with our findings, Zhang et al. (2008) demonstrated that the accuracy of source estimation decreased rapidly when the source was located outside of the grid.

Figure 6 shows the source estimates when multiple sources were simultaneously activated below the subdural

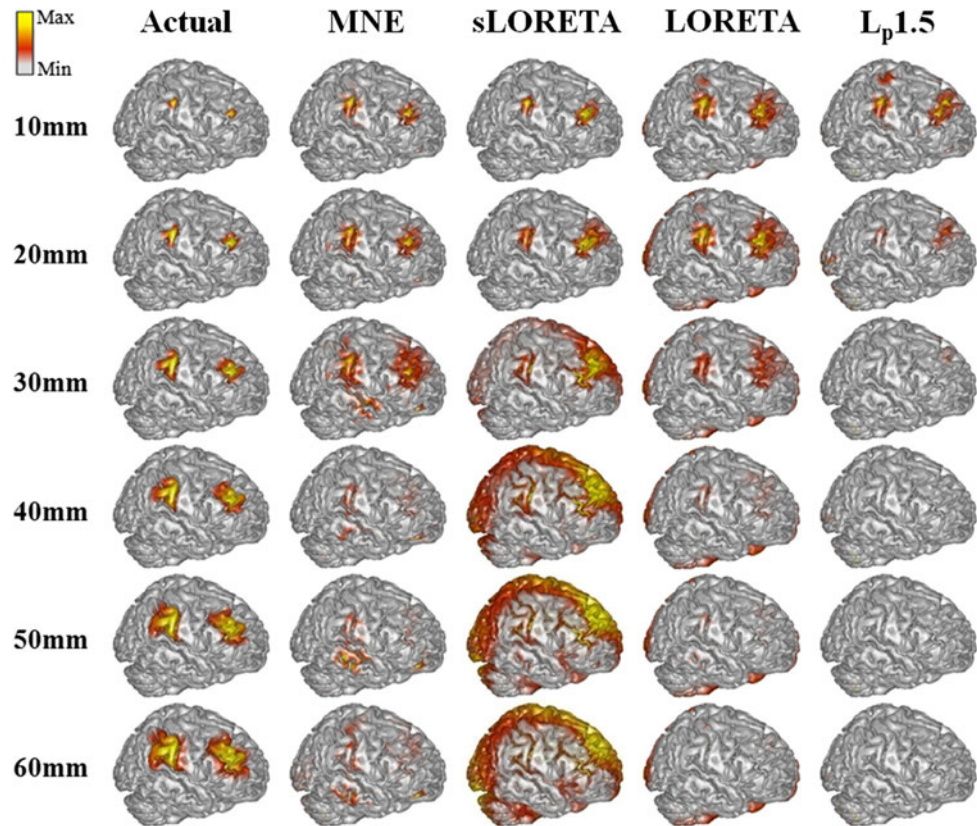
**Fig. 4** Source estimates when a single source patch was placed in the inferior parietal lobule (below the edge of the subdural grid; Case IV). Please refer to the caption of Fig. 3



**Fig. 5** Source estimates when a single source patch was placed outside the subdural grid in a relatively posterior area of the inferior parietal lobule (Case V). Please refer to the caption of Fig. 3



**Fig. 6** Source estimates when two source patches were placed at source locations 1 and 2 (both below the grid; Case VI). Please refer to the caption of Fig. 3



grid (sources 1 and 2; Case VI). In this case, the source localization accuracy decreased as the source patch radius increased, and all the results were worse than those obtained from single source simulations (Cases I–III). As in the previous simulation results, MNE provided the best estimation of the original simulated sources in all cases. Both sLORETA and LORETA were able to localize the actual source locations fairly well when the patch radius was less than 20 mm. When the patch radius exceeded 30 mm, the reconstructed source areas became larger than the previous single-source simulations. As in the previous simulation results, Lp1.5 provided the worst source estimates (the simulation results for Cases VII and VIII are shown in the Supplementary figures S3 and S4, respectively). When three sources were activated simultaneously (Case IX), even MNE was not able to successfully estimate the original source distributions for patch radii over 40 mm, and Lp1.5 was not able to localize the source activities in the right hemisphere at all (the results are shown in the Supplementary figure S5).

#### Simulation Results: Quantitative Comparison Using CC and ED

We next calculated the CC values of each simulation result for quantitative comparisons of the different imaging

algorithms (Fig. 7). High CC values indicate that the reconstructed source distribution was similar to the actual source distribution. The MNE source estimates were more accurate than those of the other algorithms, and this tendency became clearer as the source patch size increased. When the source patch was located outside the subdural grid (Fig. 7d, e), the CC values became relatively smaller than those of the other cases. In most cases, Lp1.5 yielded the smallest CC values and the sLORETA results were slightly better than the LORETA results. For small size sources with a radius smaller than 10 mm, the performances of MNE and sLORETA were similar, but the accuracy of sLORETA decreased rapidly as the patch radius increased. When multiple sources were activated simultaneously, the accuracy of source estimation decreased more rapidly than that observed for single source activation as the patch radius increased. In several cases, LORETA and Lp1.5 source estimates even showed negative correlations with the actual source distributions.

We then calculated the ED values of each simulation result for quantitative comparisons (Fig. 8). Smaller ED value indicates that the reconstructed source distribution can better identify the locations of the simulated sources. As seen in the Fig. 8, the ED results showed a similar trend with CC results. In most cases, the MNE source estimates were more accurate than those of the other algorithms, and

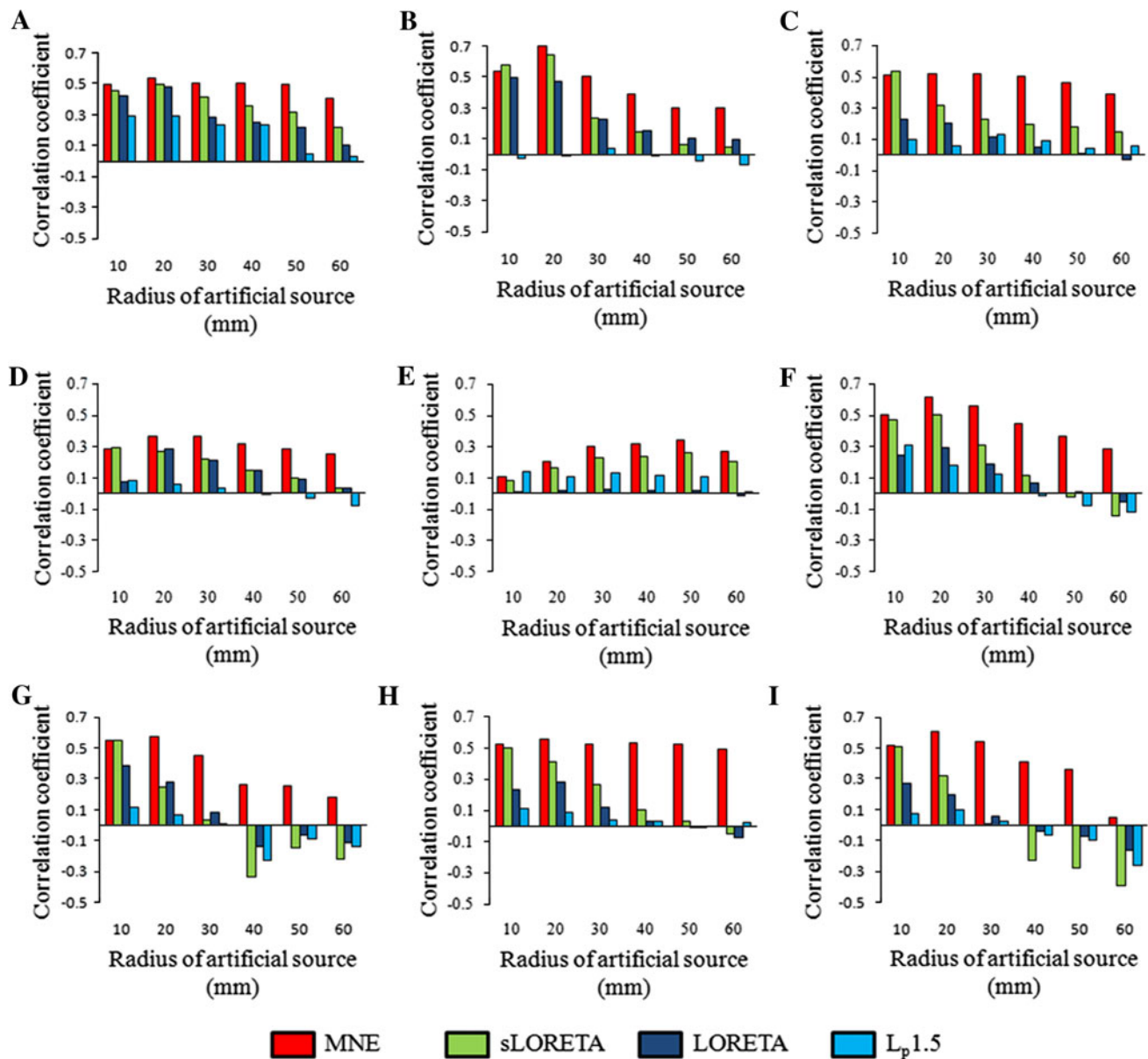


**Fig. 7** The correlation coefficient (*CC*) values for all the simulation results (Cases I–IX). Subplots A–I correspond to the results for Cases I–IX, respectively. The four different algorithms are shown in *different colors*

this tendency became clearer as the source patch size or the number of sources increased. The sLORETA results were more accurate than those of LORETA and Lp1.5, which became clearer than the previous *CC* results.

#### iEEG Source Imaging of Actual Patient Data

Figure 9a shows the locations of subdural grid electrodes implanted in the subject (LYS) as well as the surgical resection area marked on the subdural electrodes in green. Figure 9b shows a butterfly plot of the recorded iEEG signals; the red arrow indicates the analysis time slice. The source imaging results for two ictal events are illustrated in

Fig. 9c. The reconstructed source distributions showed a tendency similar to the simulation results. The MNE and sLORETA estimates covered the surgical resection area well; however, more spurious source activities in the left hemisphere were observed for the LORETA estimates. Lp1.5 was able to localize the surgical resection area fairly well, but the distribution was too focalized, consistent with a previous report (Fuchs et al. 1999). When approximating the surgical resection area on the neocortex as a circle, the radius of the circle was about 28 mm, most similar to Case I in the simulation studies. The estimation accuracies of MNE and sLORETA did not differ much for Case I when the patch radius was below 30 mm (see Figs. 7a and 8a).

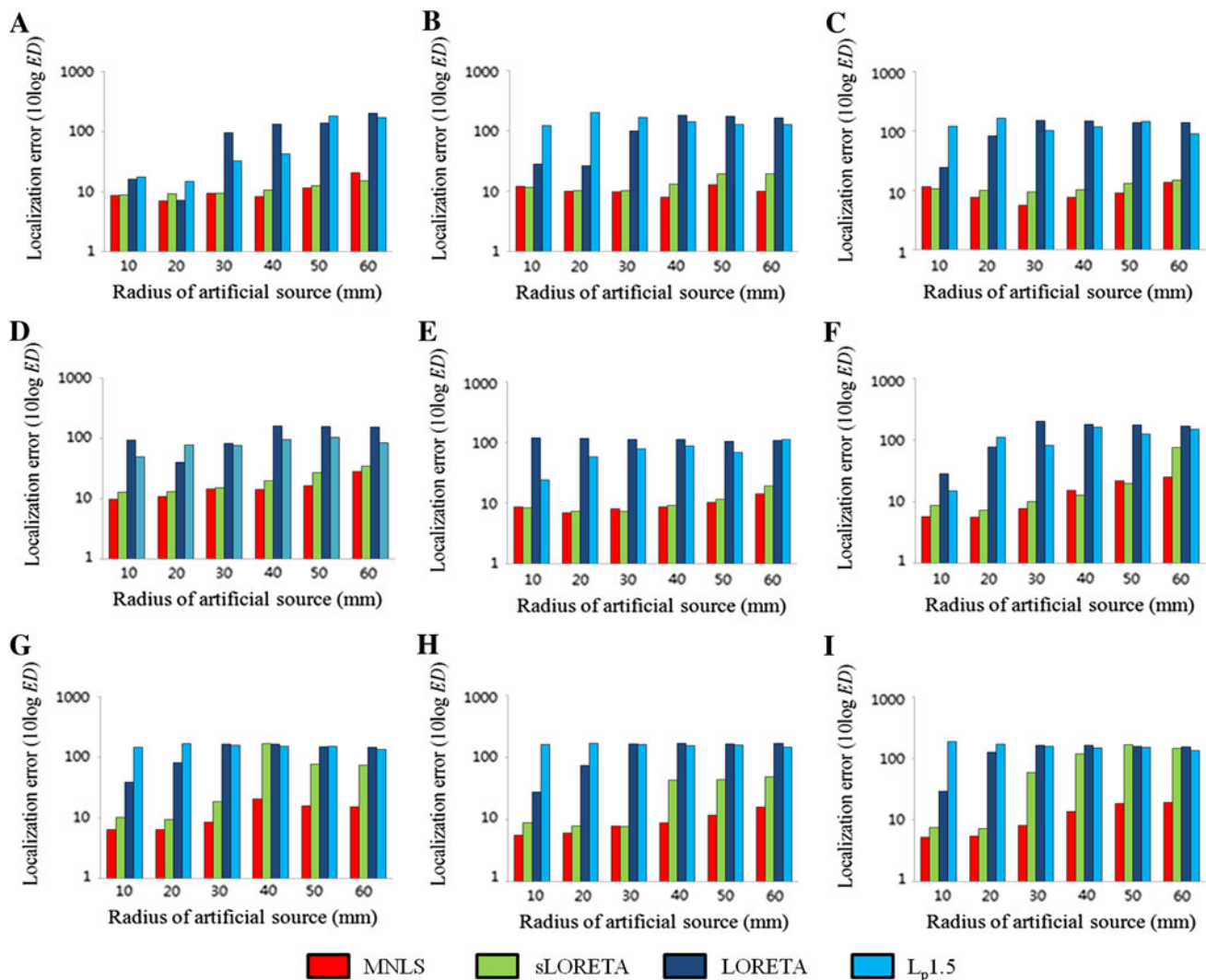


**Fig. 8** The error distance ( $ED$ ) values for all the simulation results (Cases I–IX). Subplots A–I correspond to the results for Cases I–IX, respectively. The four different algorithms are shown in *different colors*. For the visualization purpose, log scale values ( $10\log ED$ ) were used in the vertical axis

To quantify these results, we evaluated the DF values of each case, which are summarized in Table 1. The results presented in Table 1 confirm that MNE covered the resection area better than sLORETA and LORETA. The DF values of Lp1.5 source estimates were much worse than those of the other algorithms.

## Discussion

In this study, we investigated the feasibility of using iEEG-based source imaging to localize extended brain sources such as epileptogenic zones in secondary generalized epilepsy. We compared four source imaging algorithms, MNE, sLORETA, LORETA, and Lp1.5, to identify which algorithm is most appropriate for iEEG source imaging of

extended sources. In both our simulation and practical analysis studies, MNE outperformed the other imaging algorithms. The four different algorithms showed similar performances in reconstructing the original source activities when the size of the simulated source was small, demonstrating that any source-imaging algorithm can be applied successfully for source imaging of focal brain activities. The performance of the Lp1.5 algorithm decayed most rapidly of all four algorithms as the source size increased. As reported in previous studies (Zhang et al. 2008; Kim et al. 2010), the accuracy of source estimation decreases when the source is located away from the subdural grid. When multiple sources were simultaneously activated, the source estimation accuracy decreased more rapidly than when a single source was activated as the source patch size increased. When a single extended source

**Fig. 9** **a** The locations of subdural grid electrodes implanted in a subject (LYS), and the surgical resection area marked on the subdural electrodes in green; **b** A butterfly plot of the recorded iEEG signals. The red arrow indicates the analysis time slice; and **c** Source imaging results for two ictal events. All results were normalized to each maximum and displayed with a threshold of 10%

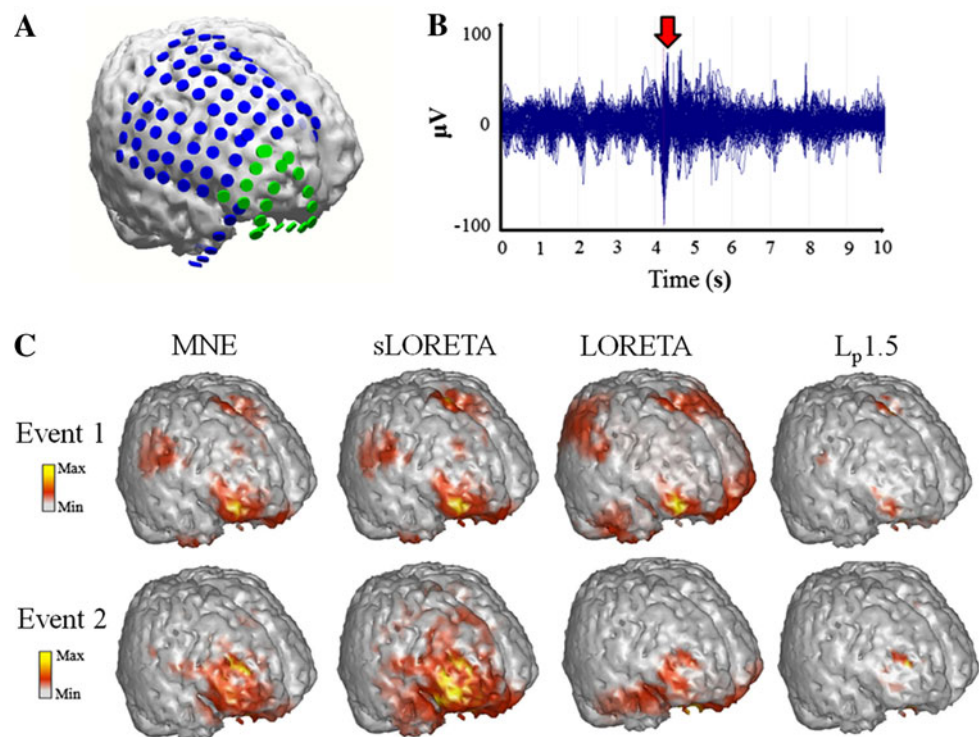


**Table 1** Degree of focalization ( $DF$ ) values evaluated for the source imaging results depicted in Fig. 9c (unit: %)

# of ictal events	MNE	sLORETA	LORETA	$L_p1.5$
1	27.23	25.78	21.74	13.55
2	38.80	35.29	15.67	9.34

was activated below the subdural grid, MNE was able to correctly localize the location of the source activation even for large extended sources with radii as large as 60 mm. Together, our results suggest that iEEG source imaging using the MNE algorithm can be used as a supplementary tool to identify extended epileptogenic zones in secondary generalized epilepsy.

In most previous EEG-based source imaging studies, LORETA-based algorithms have shown excellent performance. According to a report by Michel et al. (2004), sLORETA outperformed other algorithms, particularly in reconstructing deep brain sources. Yao and Dewald (2005) reported that the LORETA  $L_p$ -norm algorithm with  $p = 1$  gave the best source localization results among eight source imaging algorithms (minimum  $L_p$ -norm with  $p = 1, 1.5$ , and 2; LORETA  $L_p$ -norm with  $p = 1, 1.5$ , and 2, moving dipole localization with 1 or 2 sources) when focal sources with radii from 5 to 10 mm were assumed. Grova et al. (2006) showed in their simulation study that the LORETA  $L_2$ -norm-based algorithm was able to accurately reconstruct original sources with different spatial extents. Plummer et al. (2010) investigated which EEG source-imaging

algorithm was the most appropriate for the localization of epileptogenic foci in focal epilepsy. They used scalp EEG data acquired from patients with childhood benign focal epilepsy and mesial temporal lobe epilepsy and found that sLORETA showed the best performance in localizing the focal neural activities of four algorithms (MNE,  $L_1$ -norm, LORETA, sLORETA). Contrary to the results of these previous EEG studies, we found that traditional MNE-based source imaging provided the most reliable source estimates when the source activities were largely extended. These contradictory results are expected because of the intrinsic difference between iEEG and scalp EEG; in general, iEEG covers limited brain areas compared to scalp EEG. Some studies have reported that  $L_p$ -norm estimation can provide the best localization accuracy. Bai et al. (2007) evaluated different source imaging algorithms with experimental EEG datasets acquired from ten human subjects during median nerve electrical stimulation at the wrist. They demonstrated that  $L_1$ -norm based algorithms outperformed the other source imaging algorithms (MNE with  $p = 1, 1.5$ , and 2, sLORETA, and LORETA  $L_p$ -norm with  $p = 1, 1.5$ , and 2). Contrary to this report, both our simulation and experimental results showed that such focal source estimation methods might not be adequate for cortical source imaging of extended brain activities. It is noteworthy that most studies that have evaluated various source imaging algorithms have assumed different simulation or experimental conditions, such as the number of sources, electrode configurations, source sizes, and source locations. These

different conditions have often led to inconsistent or controversial results between studies. Nevertheless, all the previous evaluation studies have made important contributions to the EEG and MEG source-imaging field in that they can be used as guidelines for selecting appropriate source imaging algorithms in cases where electrophysiological datasets were recorded under similar experimental conditions to those used in particular evaluation studies. We anticipate that the results presented in this study will serve as useful guidelines for selecting appropriate algorithms for iEEG source imaging of extended sources.

In our study, a practical iEEG dataset acquired from a pediatric patient with LGS was analyzed using four cortical source-imaging algorithms. We found that the MNE results reflected the surgical resection area fairly well. Source estimates obtained using sLORETA and LORETA covered broader cortical areas (Liu et al. 2005) or contained more spurious sources than those obtained using MNE. Lp1.5 yielded source estimates that were too focal to represent the extended sources. Nevertheless, most of the cortical source-imaging algorithms considered in the present study were able to localize the surgical resection areas with fairly high localization accuracy, demonstrating that iEEG source imaging has the potential to be used as an auxiliary tool to confirm manually identified epileptogenic zones in secondary generalized epilepsy.

Further studies are required to facilitate the clinical use of iEEG source imaging. In both the simulation and experimental validation studies, BEM was used to solve forward problems of volume conduction because it provides a reasonable compromise between accuracy and computational cost (Fuchs et al. 2007; Plummer et al. 2010). Although the FEM volume conductor models used by Zhang et al. (2006, 2008) could provide more accurate forward solutions by considering the insulation effect of ECoG carrier film, further investigations to reduce the difficulties in modeling and mesh generation are needed for practical application of these models. More systematic investigation on the influence of the insulated ECoG pads on the solutions of iEEG forward and inverse problems would be an interesting future topic. Moreover, since most source imaging algorithms have been developed for EEG or MEG source imaging applications, new source imaging algorithms optimized for iEEG source imaging need to be developed. We assumed various source profiles in our simulation studies, but their locations were limited only in a unilateral cortical surface, as in the previous iEEG source imaging studies (Fuchs et al. 2007; Zhang et al. 2008; Kim et al. 2010). Simulations on more various case studies (e.g., bilateral epileptiform discharges) might provide us with a new insight on the applicability of iEEG source imaging in the future. In our experimental validation study, we used only a single patient's data as an

example of iEEG source imaging because we found it difficult to obtain iEEG datasets for LGS patients who had undergone successful epilepsy surgery and did not have cerebral infarctions or progressive underlying metabolic diseases. Experimental validation studies using a variety of iEEG datasets acquired from patients with secondary generalized epilepsy are therefore required to confirm our findings in future studies.

**Acknowledgments** This work was supported by a grant of the Korea Healthcare Technology R&D Project, Ministry for Health, Welfare & Family Affairs, Republic of Korea (A090579-0901-0000201).

## References

- Aghakhani Y, Bagshaw AP, Benar CG, Hawco C, Andermann F, Dubeau F et al (2004) fMRI activation during spike and wave discharges in idiopathic generalized epilepsy. *Brain* 127:1127–1144
- Archer JS, Abbott DF, Waites AB, Jackson GD (2003) fMRI “deactivation” of the posterior cingulate during generalized spike and wave. *NeuroImage* 20:1915–1922
- Babiloni F, Babiloni C, Carducci F, Romani GL, Rossini PM, Angelone LM, Cincotti F (2003) Multimodal integration of high-resolution EEG and functional magnetic resonance imaging data: a simulation study. *NeuroImage* 19:1–15
- Babiloni F, Cincotti F, Babiloni C, Carducci F, Mattia D, Astolfi L, Basilisco A, Rossini PM, Ding L, Ni Y, Cheng J, Christine K, Sweeney J, He B (2005) Estimation of the cortical functional connectivity with the multimodal integration of high-resolution EEG and fMRI data by directed transfer function. *NeuroImage* 24:118–131
- Bai X, Towle VL, He EJ, He B (2007) Evaluation of cortical current density imaging methods using intracranial electrocorticograms and functional MRI. *NeuroImage* 35:598–608
- Bai X, Vestal M, Berman R, Negishi M, Spann M, Vega C, DeSalvo MN, Novotny E, Constable RT, Blumenfeld H (2010) Dynamic timecourse of typical childhood absence seizures: EEG, behavior and fMRI. *J Neurosci* 30:5884–5893
- Behrens E, Zentner J, Van Roost D, Hufnagel A, Elger CE, Schramm J (1994) Subdural and depth electrodes in the presurgical evaluation of epilepsy. *Acta Neurochir* 128:84–87
- Berman R, Negishi M, Spann M, Chung MH, Bai X, Purcaro M, Motelow JE, DixCooper L, Enev M, Novotny EJ, Constable RT, Blumenfeld H (2010) Simultaneous EEG, fMRI, and behavioral testing in typical childhood absence seizures. *Epilepsia* 51:2011–2022
- Binnie CD, Elwes RDC, Polkey CE, Volans A (1994) Utility of stereoelectroencephalography in preoperative assessment of temporal lobe epilepsy. *J Neurol Neurosurg Psychiatry* 57:58–65
- Dale AM, Sereno MI (1993) Improved localization of cortical activity by combining EEG and MEG with MRI cortical surface reconstruction: a linear approach. *J Cogn Neurosci* 5:162–176
- Dale AM, Liu AK, Fischl BR, Buckner RL, Belliveau JW, Lewine JD, Halgren E (2000) Dynamic statistical parametric mapping: combining fMRI and MEG for high-resolution imaging of cortical activity. *Neuron* 26:55–67
- Dubeau F, McLachlan RS (2000) Invasive electrographic recording techniques in temporal lobe epilepsy. *Can J Neurol Sci* 27:S29–S34
- Dümpelmann M, Fell J, Wellmer J, Urbach H, Elger CE (2009) 3D source localization derived from subdural strip and grid

- electrodes: a simulation study. *Clin Neurophysiol* 120:1061–1069
- Fuchs M, Wagner M, Köhler T, Wischmann HA (1999) Linear and nonlinear current density reconstructions. *J Clin Neurophysiol* 16:267–295
- Fuchs M, Wagner M, Kastner J (2007) Development of volume conductor and source models to localize epileptic foci. *J Clin Neurophysiol* 24:101–119
- Gotman J, Grova C, Bagshaw A, Kobayshi E, Aghakhani Y, Dubeau F (2005) Generalized epileptic discharges show thalamocortical activation and suspension of the default state of the brain. *Proc Natl Acad Sci USA* 102:15236–15240
- Grova C, Daunizeau J, Lina JM, Bénar CG, Benali H, Gotman J (2006) Evaluation of EEG localization methods using realistic simulations of interictal spikes. *NeuroImage* 29:734–753
- Heiskala H (1997) Community-based study of lennox-gastaut syndrome. *Epilepsia* 38:526–531
- Im CH, An KO, Jung HK, Kwon H, Lee YH (2003) Assessment criteria for MEG/EEG cortical patch tests. *Phys Med Biol* 48:2561–2573
- Kim YK, Lee DS, Lee SK, Chung CK, Chung JK, Lee MC (2002) <sup>18</sup>F-FDG PET in localization of frontal lobe epilepsy: comparison of visual and SPM analysis. *J Nucl Med* 43:1167–1174
- Kim JS, Im CH, Jung YJ, Kim EY, Lee SK, Chung CK (2010) Localization and propagation analysis of ictal source rhythm by electrocorticography. *NeuroImage* 52:1279–1288
- Kincaes WE, Braun C, Kaiser S, Elbert T (1999) Modeling extended sources of event-related potentials using anatomical and physiological constraints. *Hum Brain Mapp* 8:182–193
- Krakow K, Woermann FG, Symms MR, Allen PJ, Lemieux L, Barker GJ, Duncan JS, Fish DR (1999) EEG-triggered functional MRI of interictal epileptiform activity in patients with partial seizures. *Brain* 122:1679–1688
- Lee YJ, Kang HC, Lee JS, Kim SH, Kim DS, Shim KW, Lee YH, Kim TS, Kim HD (2010) Resective pediatric epilepsy surgery in Lennox-Gastaut syndrome. *Pediatrics* 125:e58–e66
- Liu AK, Dale AM, Belliveau JW (2002) Monte Carlo simulation studies of EEG and MEG localization accuracy. *Hum Brain Mapp* 16:47–62
- Liu H, Schimpf PH, Dong G, Gao X, Yang F, Gao S (2005) Standardized shrinking LORETA-FOCUSS (SSLOFO): a new algorithm for spatio-temporal EEG source reconstruction. *IEEE Trans Biomed Eng* 52:1681–1691
- Michel CM, Murray MM, Lantz G, Gonzalez S, Spinelli L, Grave De Peralta R (2004) EEG source imaging. *Clin Neurophysiol* 115:2195–2222
- Nunez PL, Srinivasan R (2006) *Electric fields of the brain: the neurophysics of EEG*. Oxford University Press, New York
- Oliveira AJ, Da Costa JC, Hilário LN, Anselmi OE, Palmira A (1999) Localization of the epileptogenic zone by ictal and interictal SPECT with <sup>99m</sup>Tc-ethyl cysteinate dimer in patients with medically refractory epilepsy. *Epilepsia* 40:693–702
- Oostendorp TF, Delbeke J, Stegeman DF (2000) The conductivity of the human skull: results of in vivo and in vitro measurements. *IEEE Trans Biomed Eng* 47:1487–1492
- Pascual-Marqui RD (2002) Standardized low-resolution brain electromagnetic tomography (sLORETA): technical details. *Methods Find Exp Clin Pharmacol* 24(Suppl D):5–12
- Pascual-Marqui RD, Michel CM, Lehmann D (1994) Low resolution electromagnetic tomography: a new method for localizing electrical activity in the brain. *Int J Psychophysiol* 18:49–65
- Plummer C, Wagner M, Fuchs M, Vogrin S, Litewka L, Farish S, Bailey C, Harvey AS, Cook MJ (2010) Clinical utility of distributed source modelling of interictal scalp EEG in focal epilepsy. *Clin Neurophysiol* 121:1726–1739
- Pondal-Sordo M, Diosy D, Téllez-Zenteno JF, Sahjpal R, Wiebe S (2007) Usefulness of intracranial EEG in the decision process for epilepsy surgery. *Epilepsy Res* 74:176–182
- Rosenow F, Lüders H (2001) Presurgical evaluation of epilepsy. *Brain* 124:1683–1700
- Salek-Haddadi A, Lemieux L, Merschhemke M, Friston K, Duncan J, Fish D (2003) Functional magnetic resonance imaging of human absence seizures. *Ann Neurol* 53:663–667
- Surazhsky V, Surazhsky T, Kirsanov D, Gortler SJ, Hoppe H (2005) Fast exact and approximate geodesics on meshes. *ACM Trans Graph* 24:553–560
- Wang JZ, Williamson SJ, Kaufman L (1992) Magnetic source images determined by a lead-field analysis: the unique minimum-norm least-squares estimation. *IEEE Trans Biomed Eng* 39:665–675
- Wille C, Van Drongelen W, Kohrman M, He B (2010) Neocortical seizure foci localization by means of a directed transfer function method. *Epilepsia* 51:564–572
- Wischmann HA, Fuchs M, Dössel O (1992) Effect of the signal-to-noise ratio on the quality of linear estimation reconstructions of distributed current sources. *Brain Topogr* 5:189–194
- Wu JY, Sutherling WW, Koh S, Salamon N, Jonas R, Yudovin S, Sankar R, Shields WD, Mathern GW (2006) Magnetic source imaging localizes epileptogenic zone in children with tuberous sclerosis complex. *Neurology* 66:1270–1272
- Wyllie E, Lachhwani DK, Gupta A, Chirla A, Cosmo G, Worley S, Kotagal P, Ruggieri P, Bingaman WE (2007) Successful surgery for epilepsy due to early brain lesions despite generalized EEG findings. *Neurology* 69:389–397
- Yao J, Dewald JPA (2005) Evaluation of different cortical source localization methods using simulated and experimental EEG data. *NeuroImage* 25:369–382
- Zhang YC, Ding L, van Drongelen W, Hecox K, Frim DM, He B (2006) A cortical potential imaging study from simultaneous extra- and intracranial electrical recordings by means of the finite element method. *NeuroImage* 31:1513–1524
- Zhang YC, van Drongelen W, Kohrman M, He B (2008) Three-dimensional brain current source reconstruction from intracranial ECoG recordings. *NeuroImage* 42:683–695